






Topological and magnetic properties of the interacting Bernevig-Hughes-Zhang modelRahul Soni ^{1,2}, Harini Radhakrishnan ^{1,2}, Bernd Rosenow ³, Gonzalo Alvarez ⁴, and Adrian Del Maestro ^{1,2,5}¹*Department of Physics and Astronomy, University of Tennessee, Knoxville, Tennessee 37996, USA*²*Institute for Advanced Materials and Manufacturing, University of Tennessee, Knoxville, Tennessee 37996, USA*³*Institut für Theoretische Physik, Universität Leipzig, Brüderstrasse 16, 04103 Leipzig, Germany*⁴*Computational Sciences and Engineering Division, Oak Ridge National Laboratory, Oak Ridge, Tennessee 37831, USA*⁵*Min H. Kao Department of Electrical Engineering and Computer Science, University of Tennessee, Knoxville, Tennessee 37996, USA*

(Received 16 November 2023; accepted 2 May 2024; published 10 June 2024)

We investigate the effects of electronic correlations on the Bernevig-Hughes-Zhang model using the real-space density matrix renormalization group (DMRG) algorithm. We introduce a method to probe topological phase transitions in systems with strong correlations using DMRG, substantiated by an unsupervised machine learning methodology that analyzes the orbital structure of the real-space edges. Including the full multi-orbital Hubbard interaction term, we construct a phase diagram as a function of a gap parameter (m) and the Hubbard interaction strength (U) via exact DMRG simulations on $N \times 4$ cylinders. Our analysis confirms that the topological phase persists in the presence of interactions, consistent with previous studies, but it also reveals an intriguing phase transition from a paramagnetic to a stripey antiferromagnetic topological insulator. The combination of the magnetic structure factor, strength of magnetic moments, and the orbitally resolved density, provides real-space information on both topology and magnetism in a strongly correlated system.

DOI: [10.1103/PhysRevB.109.245115](https://doi.org/10.1103/PhysRevB.109.245115)**I. INTRODUCTION**

Topological insulators are symmetry-protected nontrivial phases of matter featuring conducting edges or surface states while remaining insulating in the bulk [1–3]. A prime example is the quantum spin Hall insulator (QSHI) [4,5], where the underlying time-reversal symmetry (TRS) protects its counterpropagating helical edge modes against nonmagnetic impurities [6–8]. Initially proposed for graphene [4,9], the QSHI gained attention after its theoretical prediction by Bernevig, Hughes, and Zhang (BHZ) [5] and subsequent experimental verification by König *et al.* [10] in two-dimensional (2D) HgTe/CdTe quantum well systems.

While extensively investigated within the framework of noninteracting models [1,2], correlation effects in these systems have drawn much attention recently [11], since the interplay of nontrivial topology and electronic correlations can unveil novel phases of matter. Particularly in the paradigmatic BHZ model, the application of dynamical mean-field theory (DMFT) to investigate correlation effects in the form of interorbital and intra-orbital Hubbard interactions has revealed an interaction-induced topological phase transition [12] from a topologically nontrivial phase to a trivial insulator. Another study using inhomogeneous DMFT combined with iterative perturbation theory on BHZ ribbons [13] has proposed a topological phase transition from a paramagnetic topological insulating phase to an antiferromagnetic Mott insulating phase. Subsequently, Budich *et al.* [14] provided the first magnetic and topological phase diagram for the interacting BHZ model using DMFT, where they considered a Hund's coupling along with inter- and intra-orbital Hubbard interactions. They found that upon increasing interactions, a noninteracting band insulating state undergoes two phase

transitions, identifying a QSH phase at intermediate interactions and a Mott insulating phase in the strongly interacting limit. The transition from the band insulating phase to the QSH phase is of first order [15]. The BHZ model with on-site Hubbard-only interaction has also demonstrated the presence of an antiferromagnetic topological insulating (AFTI) phase [16,17], while a DMFT study with strong local Coulomb interactions has postulated the presence of this phase *between* the QSH and the Mott insulating phases [18].

In addition to these interesting interaction effects, TRS-broken BHZ systems have also attracted considerable interest recently, where an in-plane Zeeman term introduced by a ferromagnetic substrate can induce a multitude of topological phenomena such as robust corner states [19,20], crystalline Weyl semimetals [21], and quantum anomalous Hall effect (QAHE) [22]. Additionally, BHZ model with long-range interactions have also demonstrated the presence of QAHE [23]. Recent Monte Carlo studies have also revealed the presence of a topological Mott insulating phase at quarter filling in the generalized spin Hall models [24,25]. For 3D topological insulators, renormalization group analyses have demonstrated the presence of a topological phase transition into an axionic insulator for strong interactions [26]. Moreover, the possibility of edge reconstruction in the BHZ model has also been studied in [27–29]. Taken together, the diverse and interesting phenomena exhibited by this relatively simple model of a topological insulator combined with advances in the density matrix renormalization group (DMRG) algorithm as applied to quasi-2D systems [30–35] motivates revisiting with a more exact treatment.

This paper explores the effects of electronic correlations on the BHZ model using a real-space DMRG method on a $N \times 4$ cylindrical geometry. We employ the full multi-orbital

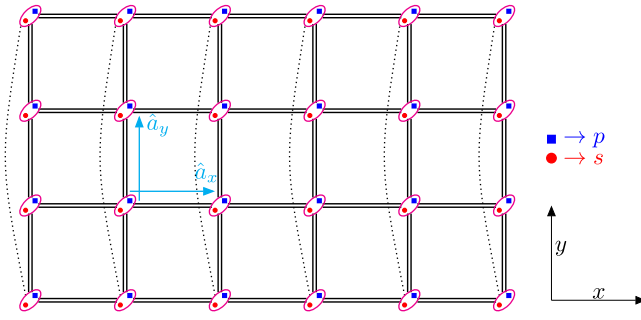


FIG. 1. Geometry of the $N \times 4$ square lattice cylinder, with $N = 6$ unit cells along the x direction and four unit cells along the y directions. Each unit cell consists of two orbitals, namely orbital s and orbital p , marked here as red circles and blue squares, respectively. The cyan arrows indicate the lattice vectors \hat{a}_x and \hat{a}_y . The dotted curves are the periodic connections along the y direction.

Hubbard interaction term involving both inter- and intra-orbital Hubbard repulsion, Hund's coupling, and a pair hopping term to study correlation effects [36–39]. Using DMRG, we find that while the overall electronic density is unchanged at the cylinder edges, we observe a characteristic increase in p -orbital density accompanied by a reduction in s -orbital density. This finding is consistent with large-scale exact diagonalization studies on the corresponding noninteracting model ($U = 0$) where the topological phase can be uniquely identify by the presence of zero energy states in the electronic spectrum localized to the edges. While it is computationally difficult to compute the electronic spectrum in the interacting model with DMRG, orbitally resolved electronic densities are readily available and provide a unique window into the presence of edges states and the accompanying correlated topological phases. By combining this orbital

analysis with local and nonlocal magnetic properties we construct a phase diagram as a function of gap parameter (m) and Hubbard interaction strength (U) for $N \times 4$ cylinder (for $N = 4, 6, 8$). Using orbital densities alone, an unsupervised machine learning approach is sensitive to the existence of two different topologically nontrivial phases, identified by an inversion of the orbital polarity of edge densities. This distinction is confirmed by an analysis of magnetic properties indicating both a paramagnetic and a topological phase with stripey antiferromagnetic correlations. The paramagnetic phase was previously identified in DMFT studies [13–15], and here we confirm the presence of a stripey antiferromagnetic topological phase intermediate between the paramagnetic QSH and Mott insulating phases as postulated in [18]. To aid in the comparison with previous foundational studies, we use the same set of parameters considered in [14,15,18].

The organization of the paper is as follows. In Sec. II, the real-space interacting BHZ model is presented along with the DMRG methodology used in this study. Section III contains the main numerical results obtained from DMRG calculations of an $N \times 4$ cylinder. Towards the end of this section, we present a complete magnetic and topological phase diagram of the interacting BHZ model using DMRG. Finally, in Sec. IV we conclude and mention a number of implications for future work.

II. MODEL AND METHOD

A. Noninteracting BHZ model

We begin our analysis by examining the real-space Hamiltonian of the BHZ model on a 2D square lattice, which is derived from the inverse Fourier transform of the original momentum-space BHZ model [5], with a specific focus on the particle-hole symmetric case. The real-space Hamiltonian [14,16,20] is given by the equation

$$\begin{aligned}
 H_0 = & B \sum_{\mathbf{r}, \alpha, \sigma} [c_{\mathbf{r}, \alpha, \sigma}^\dagger (\tau^z)_{\alpha\alpha} c_{\mathbf{r}+\hat{x}, \alpha, \sigma} + c_{\mathbf{r}, \alpha, \sigma}^\dagger (\tau^z)_{\alpha\alpha} c_{\mathbf{r}+\hat{y}, \alpha, \sigma} + \text{H.c.}] + m \sum_{\mathbf{r}} (n_{\mathbf{r}, s} - n_{\mathbf{r}, p}) \\
 & + \frac{A}{2} \sum_{\substack{\mathbf{r}, \alpha, \beta, \sigma \\ \alpha \neq \beta}} [(-1)^\sigma c_{\mathbf{r}, \alpha, \sigma}^\dagger (i\tau^x)_{\alpha\beta} c_{\mathbf{r}+\hat{x}, \beta, \sigma} + c_{\mathbf{r}, \alpha, \sigma}^\dagger (-i\tau^y)_{\alpha\beta} c_{\mathbf{r}+\hat{y}, \beta, \sigma} + \text{H.c.}], \quad (1)
 \end{aligned}$$

where $\mathbf{r} = (r_x, r_y)$ represents the unit-cell vector with components r_x and r_y along the lattice vectors \hat{a}_x and \hat{a}_y , respectively, α and β denotes the orbital indexes within the unit cell \mathbf{r} , where $\alpha, \beta = s, p$ (see Fig. 1 for details), and $\sigma = \uparrow, \downarrow$ represents the z -axis spin projection of an electron with orbital α in cell \mathbf{r} . The operator $c_{\mathbf{r}, \alpha, \sigma}^\dagger$ ($c_{\mathbf{r}, \alpha, \sigma}$) creates (annihilates) an electron with spin projection σ in orbital α at unit cell \mathbf{r} and $n_{\mathbf{r}, \alpha} = \sum_{\sigma} c_{\mathbf{r}, \alpha, \sigma}^\dagger c_{\mathbf{r}, \alpha, \sigma}$ is the local density of electrons for orbital α at unit cell \mathbf{r} . τ^x , τ^y , and τ^z are the Pauli matrices. The factor $(-1)^\sigma = -1(1)$ for $\sigma = \uparrow$ (\downarrow).

The noninteracting Hamiltonian in Eq. (1) is comprised of three separate terms. The first term describes the orbital-dependent nearest-neighbor (NN) intra-orbital hopping with amplitude B . Figure 2(a) provides an illustration of these connections, where the hopping amplitude is positive for orbital s and negative for orbital p , for both spin-up and

spin-down particles. The second term is the on-site energy term for the two orbitals, s and p . The on-site energy m is positive(negative) for orbital s (p). The last term accounts for the NN interorbital hopping, referred to as the orbital-mixing term within this study. It contains spin-dependent hopping between different orbitals and behaves similar to a NN spin-orbit coupling term. Figure 2(b) demonstrates these connections for spin-up particles along the x and y directions. Despite the presence of this pseudospin-orbit coupling like term, the single-particle Hamiltonian in equation (1) still commutes with the total S^z operator, i.e., $[H_0, S_{tot}^z] = 0$, making this model a promising candidate to study the interplay of correlation and topology with techniques such as DMRG.

In the remainder of this paper, we have adopted fixed values for the hopping amplitudes, $A = 0.3$ and $B = 0.5$ to

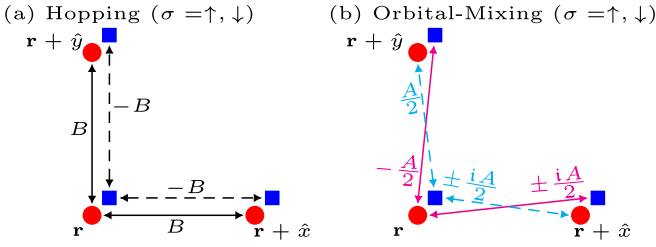


FIG. 2. (a) Depicts the nearest-neighbor intra-orbital hopping connections along the x and y directions for both spin-up and spin-down particles. The hopping connections are positive for orbital s and negative for orbital p , respectively. (b) Shows the nearest-neighbor interorbital hopping connections or orbital-mixing connections along the x and y directions for both spin-up and spin-down particles.

aid comparison with DMFT calculations corresponding to this specific parameter set [14,15,18].

B. Multi-orbital Hubbard interaction

In order to study the effects of electronic correlations, we consider the more general multi-orbital Hubbard interaction [36–39],

$$H_{\text{int}} = U \sum_{\mathbf{r},\alpha} n_{\mathbf{r},\alpha,\uparrow} n_{\mathbf{r},\alpha,\downarrow} + \left(U' - \frac{J_H}{2} \right) \sum_{\mathbf{r}} \sum_{\alpha < \alpha'} n_{\mathbf{r},\alpha} n_{\mathbf{r},\alpha'} - 2J_H \sum_{\mathbf{r}} \sum_{\alpha < \alpha'} \mathbf{S}_{\mathbf{r},\alpha} \cdot \mathbf{S}_{\mathbf{r},\alpha'} + J_H \sum_{\mathbf{r}} \sum_{\alpha < \alpha'} (P_{\mathbf{r},\alpha}^\dagger P_{\mathbf{r},\alpha'} + \text{H.c.}) \quad (2)$$

Here, the first term represents the standard on-site Hubbard repulsion U between spin \uparrow and \downarrow electrons, acting on the same orbital within a unit cell. The second term describes the on-site interorbital electronic repulsion between electrons at different orbitals within the same unit cell. The third term involves the Hund's coupling J_H that explicitly accompanies the ferromagnetic character between the orbitals. The operator $\mathbf{S}_{\mathbf{r},\alpha}$ denotes the total spin of the orbital α at cell \mathbf{r} . The last term signifies the on-site interorbital electron-pair hopping $P_{\mathbf{r},\alpha} = c_{\mathbf{r},\alpha,\uparrow} c_{\mathbf{r},\alpha,\downarrow}$. We incorporate the standard relation $U' = U - 2J_H$ and fix $J_H/U = 0.25$ [14,15,18]. The choice $J_H/U = 0.25$ facilitates a direct comparison with existing DMFT studies and is believed to be relevant for a wide range of transition metal compounds, like the iron-based superconductors [37,38].

Equations (1) and (2) constitute our interacting BHZ Hamiltonian, given by

$$H = H_0 + H_{\text{int}}. \quad (3)$$

To study this Hamiltonian numerically, we performed extensive DMRG [40,41] simulations on 4×4 and 6×4 cylinders, that correspond to 16-site two-orbitals and 24-site two-orbitals system, respectively, at half-filling. The featured systems possess open boundary conditions along the x -direction and periodic boundary conditions along the y direction. We employ the DMRG++ computer program developed by one of the authors (G.A.) [42]. To ensure proper convergence of the DMRG calculations, we consider a minimum of 1500 states and a maximum truncation error of 10^{-5}

throughout the finite algorithm sweeps. By adhering to these criteria, we obtain essentially exact ground-state properties, which are used to identify magnetic and topological features and phases of the interacting BHZ model. A particular case of the interacting BHZ model shown in (3) has also been studied for spinless fermions in [43,44].

III. RESULTS

A. Noninteracting $U = 0$

To aid in the interpretation of interaction effects, we begin by examining the real-space BHZ model at $U = 0$ at half-filling on a $N \times 4$ cylinder, evaluating key topological properties via exact diagonalization. In the case of $U = 0$, the system clearly shows a topological phase transition from a nontrivial topological phase T_1 to a trivial band insulator phase BI, as depicted in Fig. 3(a) where we plot the single-particle energy eigenvalues for a 20×4 cylinder. Here, the topological phase T_1 is characterized by the presence of degenerate zero-energy modes for a range of $m \in (0, 2]$, a hallmark of the QSHI phase in HgTe/CdTe quantum wells described by the BHZ model [5], whereas the band insulator, BI, has a clear gap [with approximate size $2(m - 2)$].

To understand how the energy spectrum corresponds to physics at the sample boundary, Fig. 3(b) shows the edge electronic charge density $\langle \tilde{n}_{i,\alpha} \rangle$ of a 6×4 cylinder, which is obtained by subtracting the average charge density of the bulk from the charge density at each cell. More specifically we compute

$$\langle \tilde{n}_{i,\alpha} \rangle = \langle n_{i,\alpha} \rangle - \frac{1}{N_b} \sum_{i \in \text{bulk}} \langle n_{i,\alpha} \rangle, \quad (4)$$

where N_b corresponds to the number of unit cells in the bulk of the cylinder [as highlighted in Fig. 3(c)] and $i = r_y + L_y * r_x$ is a flattened unit-cell index. The edge charge density will act as a topological marker for the cylindrical system in both the interacting and noninteracting case. The fundamental idea is to examine the extent and character of the electronic charge density on the edges in comparison to the bulk. In Fig. 3(b), we plotted this quantity for two different values of m at $U = 0$. The figure clearly illustrates that the edge charge density is quite large for $m = 1.75$ (filled symbols), which lies in the topological T_1 phase, as compared to $m = 3.0$ (open symbols), which lies in the nontopological BI phase. Moreover, these densities are equal and opposite for both orbital s and orbital p on either edges of the cylinder. The steps in density observed for $m = 1.75$ are indicative of a physical edge states, which possess decaying real-space wavefunctions [19,45,46]. The presence of a finite-edge density is indicative of the presence of the zero-energy modes, which we expect to be true even in the presence of interactions where the bulk-boundary correspondence still holds [47].

B. Interacting $U > 0$

Having understood the emergent real-space structure of gapless edge states in the noninteracting model, we now discuss DMRG results of the interacting BHZ model on $N \times 4$ cylinders.

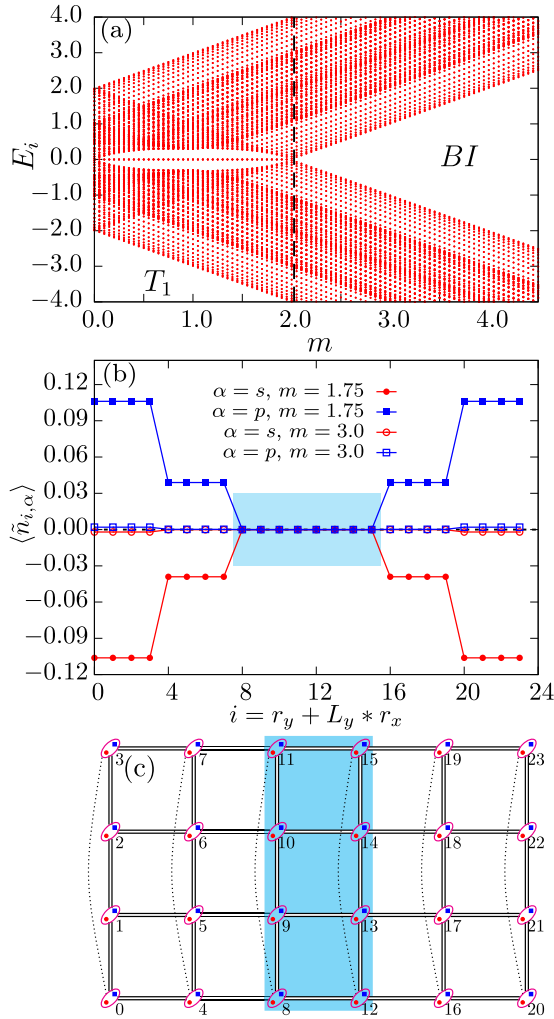


FIG. 3. (a) Plot of single-particle energy eigenvalues vs the on-site energy m at $U = 0$ for a 20×4 cylinder. The figure illustrates the presence of two phases: a nontrivial topological phase T_1 and a trivial band insulator BI at $U = 0$. (b) Reduced electronic charge density Eq. (4) at half-filling plotted vs the cell-index (i) for 6×4 cylinder at $m = 1.75$ and $m = 3.0$ within the T_1 phase and BI phase, respectively, exhibiting the localization of zero-energy modes on the edges in T_1 phase. The cyan box indicates the bulk cells of the cylinder. (c) Lattice geometry of the 6×4 BHZ cylinder with numbered unit cells where the bulk cells are highlighted in cyan.

In the subsequent subsections, we present interaction results for both 8×4 and 4×4 cylinders. We begin by demonstrating the consistency of results for both cylinder sizes for a fixed value of the on-site energy $m = 3.0$, as a function of increasing U . Next, we showcase results for $m = 1.75$ in the context of a 4×4 cylinder. Owing to the significant computational cost of $N = 8$ and the finite-size convergence study presented in Appendix B, a majority of results are confined to $N = 4$.

1. Charge and magnetic properties

We begin our analysis by focusing on more conventional local and nonlocal charge and magnetic properties of the system. We first fix $m = 3.0$, deep in the BI phase at $U = 0$,

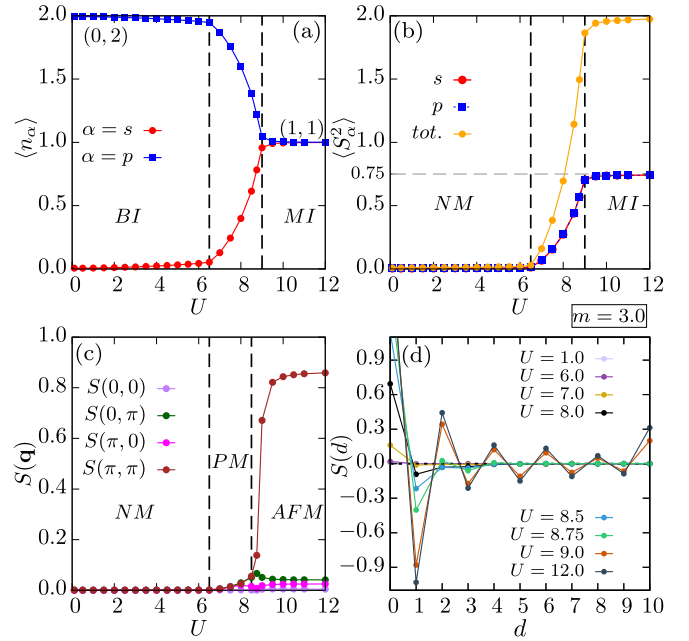


FIG. 4. Charge and magnetic properties of the interacting BHZ model with $m = 3.0$, $U \geq 0$ on a 8×4 cylinder. (a) Average orbital occupation $\langle n_\alpha \rangle$ plotted vs U for both orbitals. The plot clearly depicts a change in orbital occupation from a $(0,2)$ band insulator configuration to $(1,1)$ Mott insulator (MI) configuration as interaction strength is increased. (b) Average magnetic moment of an orbital $\langle S_\alpha^2 \rangle$ and of the cell $\langle S_{tot}^2 \rangle$ plotted vs U . The plot shows a magnetic transition from a nonmagnetic (NM) phase to a magnetic phase at $U = 6.5$. (c) Spin structure factor $S(\mathbf{q})$ showing the transition from NM to PM to AFM phase as we increase U . (d) Real-space spin-spin correlations plotted vs the distance between spins.

and increase U from the weak to strong coupling regime on a 8×4 cylinder. Local charge properties can be quantified through the average occupation of orbitals,

$$\langle n_\alpha \rangle = \frac{1}{N_c} \sum_{\mathbf{r}} \langle n_{\mathbf{r},\alpha} \rangle, \quad (5)$$

where N_c is the total number of unit cells. Figure 4(a) illustrates the average orbital occupation versus the interaction strength. The plot demonstrates that as we increase U from the weak- to the strong-coupling regime, the system transitions from a $(n_s, n_p) = (0, 2)$ configuration of a band insulator (BI) towards a $(1,1)$ Mott insulator (MI). Between these two insulating phases, beginning near $U = 6.5$ we observe a $(n, 2 - n)$ configuration [48], which uniformly changes as we increase the interaction strength until $U = 9.0$, where n is the average occupation of orbital s at interaction strength U . This is consistent with previous DMFT results [14], where a similar behavior in the average charge occupation was also observed.

For local magnetic properties, we study the average magnetic moment of the individual orbitals and the average magnetic moment of the entire unit cell,

$$\langle S_\alpha^2 \rangle = \frac{1}{N_c} \sum_{\mathbf{r}} \langle \mathbf{S}_{\mathbf{r},\alpha} \cdot \mathbf{S}_{\mathbf{r},\alpha} \rangle, \quad (6)$$

$$\langle S_{tot}^2 \rangle = \frac{1}{N_c} \sum_{\mathbf{r}} \langle \mathbf{S}_{\mathbf{r}} \cdot \mathbf{S}_{\mathbf{r}} \rangle, \quad (7)$$

where $\mathbf{S}_r = \sum_{\alpha} \mathbf{S}_{r,\alpha}$. Figure 4(b) shows the average magnetic moment of the individual orbitals as well as the total for the unit cell as a function of interaction strength at $m = 3.0$. The plot shows that the BI phase—present for $U \leq 6.5$ —is also nonmagnetic (NM), as the average magnetic moments for both orbitals and the unit cell is vanishingly small. For $U > 6.5$, the system attains magnetism, and upon increasing interactions the average magnetic moment of the orbitals smoothly increases until it saturates to 0.75 in the (1,1) configuration of the Mott insulator for $U > 9.0$. Additionally, the magnetic moment for both orbital s and orbital p fall directly on top of each other for all values of U in Fig. 4(b); this feature is observed to be true for all values of m .

Finally, to explore nonlocal magnetic properties, we compute the real-space spin-spin correlation $S(d)$ defined as

$$S(d) = \frac{1}{\#(d)} \sum_i \langle \mathbf{S}_i \cdot \mathbf{S}_{i+d} \rangle, \quad (8)$$

and the corresponding spin structure factor $S(\mathbf{q})$,

$$S(\mathbf{q}) = \frac{1}{4N_c^2} \sum_{\mathbf{r}, \mathbf{r}', \alpha, \beta} e^{-i\mathbf{q} \cdot (\mathbf{r} - \mathbf{r}')} \langle \mathbf{S}_{\mathbf{r},\alpha} \cdot \mathbf{S}_{\mathbf{r}',\beta} \rangle, \quad (9)$$

where $\#(d)$ is the number of sites separated by the distance d . The structure factor is shown in Fig. 4(c), and it provides a clear picture of the magnetic phases in the system: (i) It confirms the presence of the NM phase for $U \leq 6.5$, (ii) for $6.5 < U < 8.5$ the system is paramagnetic (PM) as there is no dominant magnetic ordering present; and (iii) for $U \geq 8.5$ the system is antiferromagnetic (AFM) with dominant (π, π) ordering. Additionally, it is worth pointing out that the AFM correlations appears before than the MI phase: AFM ordering is observable at $U = 8.5$, while the MI appears for $U > 9.0$. Note that the vertical-dashed lines in Figs. 4(a)–4(c) serve as an indicator of a qualitative change in observed quantities and do not represent a thermodynamic limit phase boundary.

Figure 4(d) presents a real-space picture of the magnetic and nonmagnetic phases for fixed $m = 3.0$. The spin-spin correlations also provides a confirmation of the paramagnetic (PM) phase, where $S(d)$ lacks any signatures of long-range ordering. Additionally, it highlights the onset of the antiferromagnetic (AFM) phase at $U = 8.5$. We note that the spin-spin correlations are computed for the entire cells, and we have observed a consistent behavior across individual orbitals for all magnetic and nonmagnetic regimes within our calculations. We note that interaction results, covering both the charge and magnetic properties discussed in this section, as well as the topological properties addressed in the subsequent section for $m = 3.0$ in 8×4 cylinders are in alignment with those observed for their 4×4 counterparts. The equivalent results for the smaller cylinders are included in Appendix C for completeness.

We next present analogous results for a smaller value of $m = 1.75$ on a 4×4 cylinder in Fig. 5, where the noninteracting model lies within the topological T_1 phase at $U = 0$. By increasing U , we explore the effects of interactions and find that in contrast to the case of $m = 3.0$, for $m = 1.75$, there is no evidence of a nonmagnetic BI phase. This can be observed in panel (a), where the orbital densities are never saturated for small U , and instead they continuously move towards the (1,1)

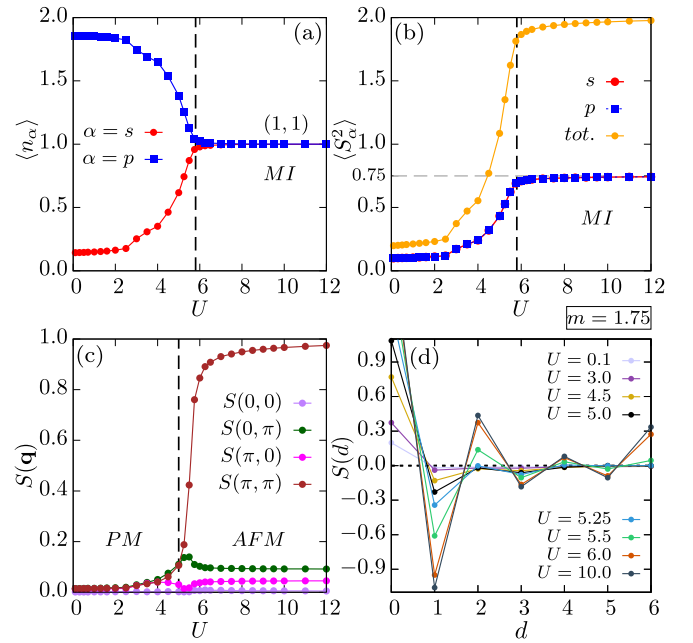


FIG. 5. Charge and magnetic properties of the interacting BHZ model at $m = 1.75$, $U > 0$ on a 4×4 cylinder. (a) Average orbital occupation vs U for both orbital s and orbital p . The orbital occupation changes towards a (1,1) Mott insulator (MI) configuration as U increases. (b) Average magnetic moment of orbitals and the unit cell as a function of U showing the evolution of the moments from paramagnetic (PM) phase to the MI phase. (c) Spin structure factor $S(\mathbf{q})$ vs U providing evidence of the magnetic phase transition from PM to an antiferromagnetic Mott insulating (AFM MI) phase as U increases. (d) Real-space spin-spin correlations plotted vs the distance between spins.

occupations characteristic of the Mott insulating phase, which develops near $U = 6.0$. The accompanying magnetic moments shown in panel (b) are also distinct from $m = 3.0$, where the strictly nonmagnetic region is never observed with $\langle S_{\alpha}^z \rangle > 0$ for all $U \geq 0$. Furthermore, an analysis of the spin structure factor in panel (c) shows that the PM phase persists until nearly $U = 5.0$. However, here we do observe a similarity with $m = 3.0$ case, as a weak AFM phase develops, after the PM phase, for $U \geq 5.0$, which continues until it merges into the more robust antiferromagnetic Mott insulating phase at $U = 6.0$. The resulting real-space spin-spin correlations in panel (d) are also larger in the strong interaction limit.

2. Topological properties

Motivated by our analysis for the noninteracting BHZ model with $U = 0$, we employ the edge electronic charge density defined in Eq. (4) as a key property for the characterization of the topological phases with interaction. In Fig. 6(a), we illustrate this quantity for three different values of $U = 1.0, 7.0$ and 8.5 at $m = 3.0$ for a 8×4 cylinder. The interaction $U = 1.0$ (open symbols) falls in the band insulating region, as discussed previously. The edge electronic charge density at this parameter value is almost negligible supporting the conclusion that the band insulator is trivial. Conversely, for $U = 7.0$ (solid points/lines), the system is in the paramagnetic

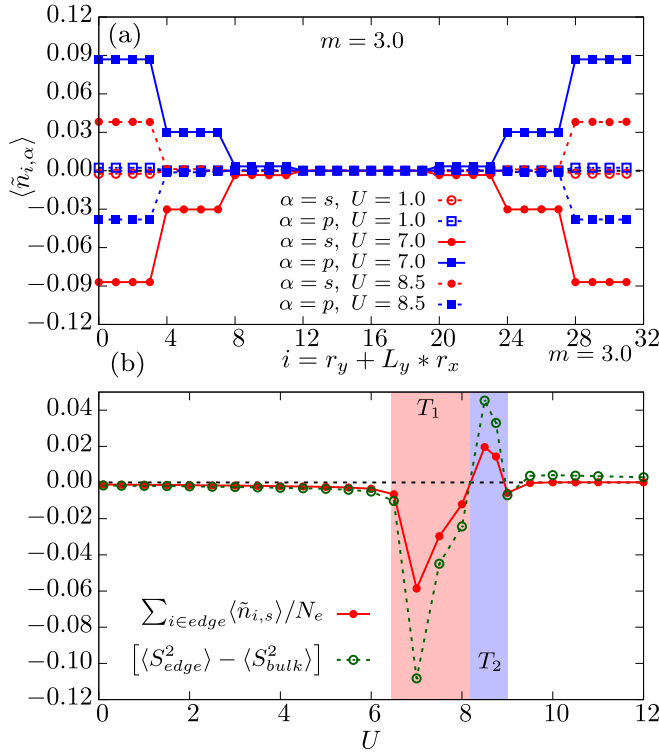


FIG. 6. Topological properties of the interacting BHZ model at $m = 3.0$ for a 8×4 cylinder. (a) Edge electronic charge density vs the cell index i for $U = 1.0, 7.0, 8.5$. The plot shows that the parameter point $U = 1.0$ is nontopological or trivial, whereas the parameter points $U = 7.0$ and 8.5 are topological. Additionally, the polarity of the edge density for orbital $s(p)$ are negative (positive) and positive (negative) at $U = 7.0$ and 8.5 , respectively, suggesting two different topological phases T_1 and T_2 . (b) Averaged edge density for orbital s and the difference of edge and bulk magnetic moments plotted vs the interaction strength U . The plot shows the change in polarity of the edge density at $U \approx 8.2$ as it moves from the T_1 to T_2 topological phase. The plot also depicts that the T_1 phase is dominated by the bulk magnetic moments, while the T_2 phase is dominated by the edge magnetic moments.

region and exhibits finite-edge density, indicating a nontrivial topology. The polarity of the edge-electronic charge density (relative signs of $\langle \tilde{n}_{i,s} \rangle < 0 < \langle \tilde{n}_{i,p} \rangle$ for $i \in \text{edge}$) at $U = 7.0$ is consistent with the T_1 phase from our noninteracting results. More interestingly, accompanying the onset of antiferromagnetic order near $U = 8.5$ (solid points, dashed lines), we observed nontrivial topological behavior in the edge electronic density, but with opposite orbital polarity as compared to the T_1 phase at $U = 7.0$. i.e. $\langle \tilde{n}_{i,p} \rangle < 0 < \langle \tilde{n}_{i,s} \rangle$ for $i \in \text{edge}$. We use this polarity inversion to infer the existence of a topological T_2 phase, which exhibits a stripey AFM order as characterized by an asymmetry in the structure factors $S(0, \pi)$ and $S(\pi, 0)$.

This inversion is quantified in Fig. 6(b), where we have computed the edge density for the orbital s , averaged over all the unit cells situated on the edges (N_e) of the cylinder and plotted it versus the interaction strength U . The result clearly illustrates a distinct polarity change, transitioning from

negative to positive, in the edge density of orbital s as the system magnetically transforms from the paramagnetic region towards the onset of antiferromagnetic order. We take this as evidence indicative of a T_1 to T_2 topological phase transition.

This change is also accompanied by a difference in magnetic moments of the edge and bulk, which follows the same pattern as the averaged edge electronic charge density. This can be quantified by defining

$$\Delta S = \langle S_{\text{edge}}^2 \rangle - \langle S_{\text{bulk}}^2 \rangle \quad (10)$$

where

$$\langle S_{\text{edge}}^2 \rangle = \frac{1}{N_e} \sum_{i \in \text{edge}} \langle S_i^2 \rangle, \quad (11)$$

$$\langle S_{\text{bulk}}^2 \rangle = \frac{1}{N_b} \sum_{i \in \text{bulk}} \langle S_i^2 \rangle. \quad (12)$$

ΔS is shown as a function of interaction strength in Fig. 6(b), where we observe that the T_1 phase is dominated by the magnetic moments of the bulk, in contrast to the T_2 phase, which exhibits larger magnetic moments along the edges. This can be intuitively understood by appealing to a real-space picture, as the antiferromagnetism first develops on the edges and then moves towards the bulk as U increases, and eventually reaches a saturation in the Mott insulating region [18]. The presence of the antiferromagnetic ordering and topology has previously been explored at the mean-field level in these systems [16–18]. We note that this subtle yet finite feature has a one-to-one connection with the edge electronic density as depicted in the figure. Similar to the case of charge and magnetic properties for $m = 3.0$, we also find a consistency in the topological properties between the 8×4 and 4×4 cylinders depicted in Appendix C.

Figure 7 presents these topological quantities for the case of $m = 1.75$ on a 4×4 cylinder. Similar to the observations made for the case of $m = 3.0$, we first identify the T_1 topological phase within the paramagnetic region, followed by the emergence of T_2 topological phase during the onset of antiferromagnetic order. The difference in magnetic moments of the edge and bulk also follows the same behavior as shown previously for the case of $m = 3.0$, that is, the paramagnetic T_1 region is dominated by the bulk moments whereas the antiferromagnetic T_2 phase is dominated by the edge moments. Moreover, our results also illustrate that the edge electronic charge density in the antiferromagnetic Mott insulating region is negligible, implying that this region is nontopological.

3. DMRG phase diagram of the interacting BHZ model

Utilizing the analysis presented in the preceding two subsections for the identification of the magnetic and topological phases, we have generated a DMRG phase diagram of the interacting BHZ model. The result, presented in Fig. 8 shows the phases as a function of the gap parameter m and the interaction strength U for $N \times 4$ cylinders with $N = 4, 8$.

For increasing interaction strength U and gap parameter $m \geq 2$, the sequence of phases is similar. Starting with weak interactions, now there is a nonmagnetic band insulating phase (green), which undergoes a transition to a paramagnetic topological phase T_1 (red) followed by a narrow region of stripey antiferromagnetic topological T_2 phase for intermediate

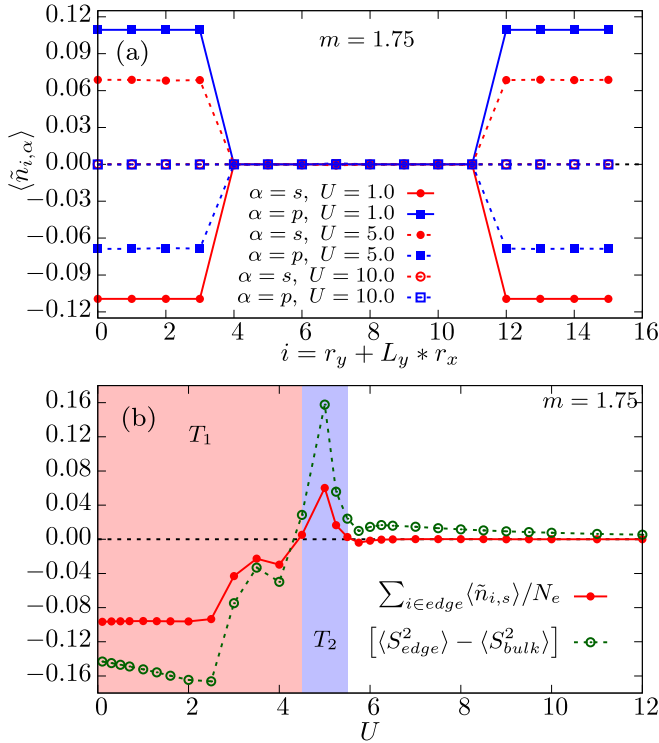


FIG. 7. Topological properties of the interacting BHZ model at $m = 1.75$ for a 4×4 cylinder. (a) Edge electronic charge density vs the cell index i for different values of U ($= 1.0, 5.0, 10.0$). The plot illustrates that paramagnetic point $U = 1.0$ lies in T_1 topological phase, whereas $U = 5.0$ lies in the T_2 topological phase. Additionally, the point $U = 10.0$, which lies in the Mott insulating region is nontopological. (b) Plot of averaged edge density for orbital s and the difference of edge and bulk magnetic moments vs the interaction strength U . The T_1 phase covers the entire paramagnetic region and transitions to the T_2 phase along with the onset of antiferromagnetic order. The entire Mott insulating region is observed to be nontopological.

coupling strengths. Lastly, there is an antiferromagnetic Mott insulating phase in the strong coupling regime. On the other hand, for $0 < m < 2$ the nonmagnetic band insulator at weak coupling is not observed. Here, with increasing interaction strength, we find a paramagnetic topological insulating T_1 region, followed by a narrow region of stripey antiferromagnetic topological insulating T_2 phase, which turns into a robust antiferromagnetic Mott insulator for strong interactions. In Fig. 8, the phase boundaries separate measured points in distinct phases. The overall distinction between topological and nontopological phases is consistent with a previous DMFT study [14]. However, here the DMRG allows us to resolve the stripey AFM correlations in the topological phase near the boundary to the AFM Mott insulator.

To compute the phase diagram, we adhered to the convergence criteria outlined in our method Sec. II. The majority of our DMRG simulations (indicated as small solid/empty circles) are for 4×4 cylinders; however, we have verified the robustness of the observed phases for larger 8×4 cylindrical systems (highlighted with with gray shading). Details of our finite-size scaling analysis are included in Appendix B. It is

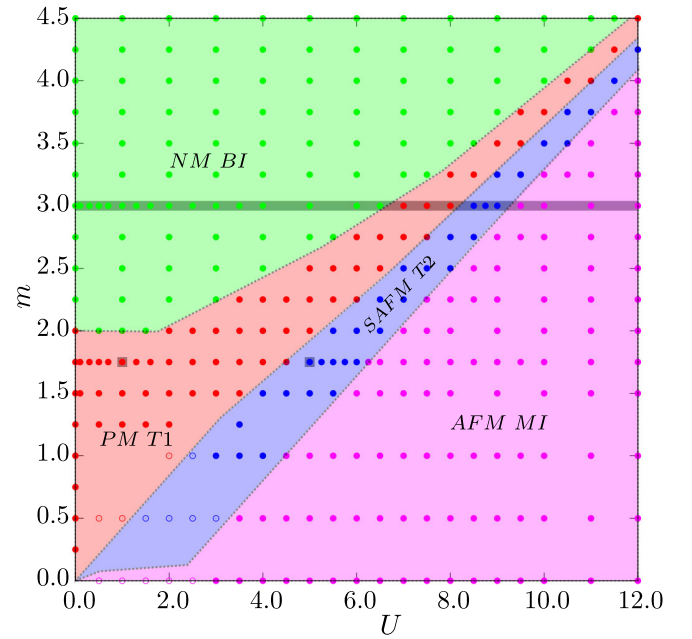


FIG. 8. Magnetic and topological phase diagram (m vs U) of the interacting BHZ model for the $N \times 4$ cylinder, using DMRG. The green region is the nonmagnetic trivial band-insulating phase, the red region is the paramagnetic topological T_1 phase, the blue region is the topological T_2 phase with stripey antiferromagnetic correlations, and the magenta region is the nontopological AFM MI phase. Circles represent simulations for 4×4 cylinders, gray squares and the entire strip at $m = 3.0$ were performed for 8×4 cylinders. Solid points indicate DMRG results fully satisfying the convergence criteria detailed in Sec. II, while open circles are for parameters where achieving complete convergence of all observables is challenging.

important to note that the solid circles indicate well-converged DMRG points, while the empty circles signify points that did not converge effectively.

4. Verification of the phase diagram using unsupervised machine learning

As our analysis of topological properties was made without direct access to the energy spectrum, we further verify the phase diagram in Fig. 8 through an unsupervised machine learning approach. We constructed a data set from each point on the phase diagram, where we assign a concatenated array of the edge electronic charge density $\langle \tilde{n}_{i,\alpha} \rangle$ at each cell index for both the s and p orbitals. Principal component analysis (PCA) [49–52] can be used to reduce the dimensionality of the data by identifying the mutually orthogonal directions along which the data varies the most through a linear combination of the original coordinates. We use the SCIKIT-LEARN package in Python [53] to identify the direction of variation with the most variability. Figure 9 depicts each point on the phase diagram colored according to the value of its first principal component, or position along the primary axis. Radial basis function interpolation is used to extrapolate the remaining segments of the phase diagram. Our analysis revealed that, while the band and Mott insulating phases exhibit similar alignment

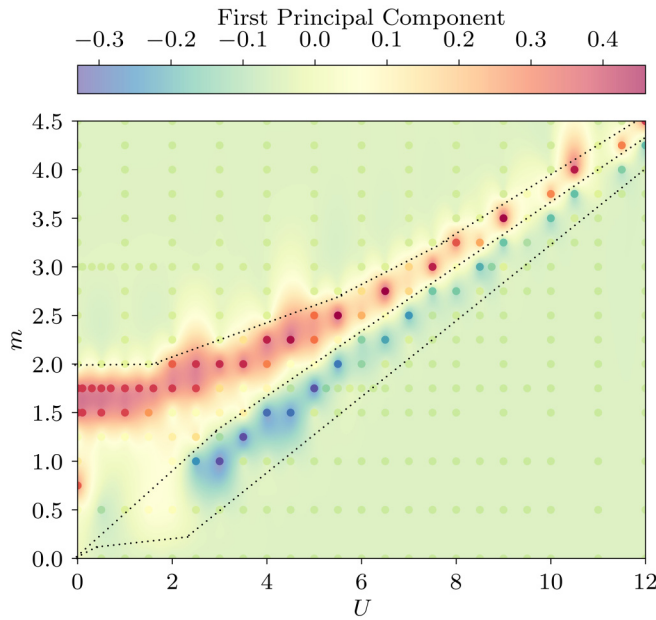


FIG. 9. Unsupervised machine learning phase diagram (m vs U) of the interacting BHZ model on a $N \times 4$ cylinder colored by the value of the first principal component obtained from principal component analysis of the edge electronic charge densities. The green regions are comprised of the band and Mott insulating phases while the region with the red and blue points correlates with the topological phases in Fig. 8. Radial basis function interpolation is used to extrapolate the remainder of the diagram. Dotted lines are the same phase boundaries inferred from Fig. 8.

along the axis, the first principal component is clearly able to identify different signatures of the two topological phases, corresponding to a strong positive or negative signal. The use of spatially resolved raw orbital density data as input strongly supports their correlation with topological properties.

IV. CONCLUSIONS

This paper has addressed the challenge of incorporating electron-electron interactions into models of topological insulators. In particular we have proposed and carried out a simulation and analysis method to understand the effects of electronic correlations on the Bernevig-Hughes-Zhang model on a $N \times 4$ cylinder, using a numerically exact real-space density matrix renormalization group (DMRG) algorithm. By combining conventional magnetic order parameters and response functions with a real-space investigation of orbitally resolved densities, we describe the interplay between topological order and pronounced interaction effects emerging at the sample boundary. The observed signature of topological order, manifest in the electronic orbital polarization near the edge, opens a route for the study of strongly interacting topological systems via DMRG. This analysis is supplemented via an unsupervised machine learning approach considering unlabelled spatial orbital occupancies as features.

Our approach, which includes the full multi-orbital Hubbard interaction term, unveils a rich magnetic and topological phase diagram as a function of gap parameter (m) and

interaction strength (U). At half-filling, our phase diagram reaffirms the existence of various magnetic and topological phases under the influence of interactions, in agreement with prior DMFT studies [14], but also provides evidence for the presence of a more subtle antiferromagnetically ordered topological insulator [16–18].

While understanding the influence of interactions in topological matter remains a considerable challenge, the DMRG framework presented here may enable further theoretical and experimental exploration of strongly correlated topological insulators.

All data, code, and analysis scripts that support the findings of this study can be found online [54].

The DMRG++ code used in this study is available on GitHub [55].

ACKNOWLEDGMENTS

R.S., H.R., and A.D.M. acknowledge support from the US Department of Energy, Office of Science, Office of Basic Energy Sciences, under Award No. DE-SC0022311. B.R. acknowledges support from the German Research Foundation under Grant RO 2247/11-1 and the hospitality of the University of Tennessee, where a portion of this work was performed. The US Department of Energy, Office of Science, National Quantum Information Science Research Centers, Quantum Science Center has supported G.A., who contributed to the DMRG aspects in this paper. R.S. acknowledges the Office of Information Technology (OIT) at the University of Tennessee for providing additional computational resources to carry out this project. The authors would like to thank F. Heidrich-Meisner, H. Barghathi, P. Laurell, and E. Dagotto for useful discussions.

APPENDIX A: SINGLE-CELL PICTURE OF THE INTERACTING BHZ MODEL

The effective Hamiltonian of an interacting unit cell with two orbitals (s and p) is expressed as

$$\begin{aligned}
 H_{\text{eff}} = & m(n_s - n_p) + U(n_{s,\uparrow}n_{s,\downarrow} + n_{p,\uparrow}n_{p,\downarrow}) \\
 & + \left(U' - \frac{J_H}{2} \right) n_s n_p - 2J_H(\mathbf{S}_s \cdot \mathbf{S}_p) \\
 & + J_H(P_s^\dagger P_p + \text{H.c.})
 \end{aligned} \tag{A1}$$

This single-cell picture of the interacting BHZ model can be analyzed to obtain an intuition and understanding of the origin of the magnetic phases present in the interacting phase diagram in Fig. 8. While Eq. (A1) does not have any hopping connections, nor does it have any reference point to identify a paramagnetic or antiferromagnetic phase, the Hamiltonian does still provide relevant information about the roles played by individual terms.

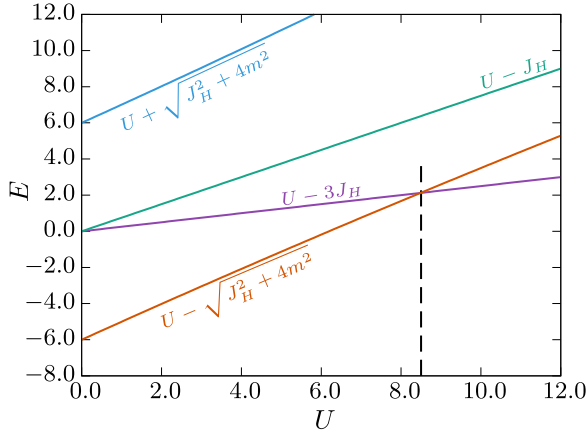


FIG. 10. Eigenvalues of an interacting unit cell vs interaction strength U for $m = 3.0$. The red and cyan lines represent the two-band insulating states $|B_1\rangle$ and $|B_2\rangle$, respectively. The purple and green lines depict the spin-triplet and singlet states, respectively. The plot shows the transition of the ground state from a nonmagnetic band-insulating state to a magnetic spin-triplet state at $U \simeq 8.5$ also indicated with a vertical-dashed line.

At half-filling, one can write the matrix form of this effective Hamiltonian using the following spin-basis $|s, p\rangle := \{|\uparrow, \downarrow\rangle, |\downarrow, \uparrow\rangle, |\uparrow\downarrow, 0\rangle, |0, \uparrow\downarrow\rangle\}$ as

$$(H_{\text{eff}}) = \begin{pmatrix} U' & -J_H & 0 & 0 \\ -J_H & U' & 0 & 0 \\ 0 & 0 & U + 2m & J_H \\ 0 & 0 & J_H & U - 2m \end{pmatrix}. \quad (\text{A2})$$

Now let us understand the components of the Hamiltonian individually. The gap term alone ($U = J_H = 0$) favors the $(n_s, n_p) = (0, 2)$ configuration and thus dominates in the weakly interacting regime, whereas the Hubbard term by itself favors the $(1, 1)$ configuration and takes over for strong

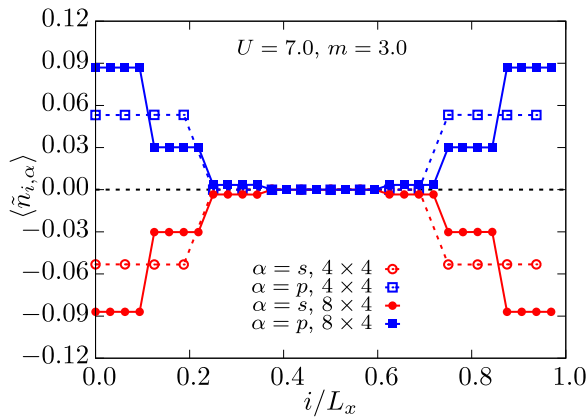


FIG. 11. Edge electronic charge density vs the relative distance along the cylinder (i/L_x) for 8×4 (filled) and 4×4 (open symbols) systems using DMRG at $U = 7.0$ and $m = 3.0$. Parameters are chosen such that the system lies within the paramagnetic T_1 phase. A finite-orbital occupancy at the edge persists for the largest systems measured.

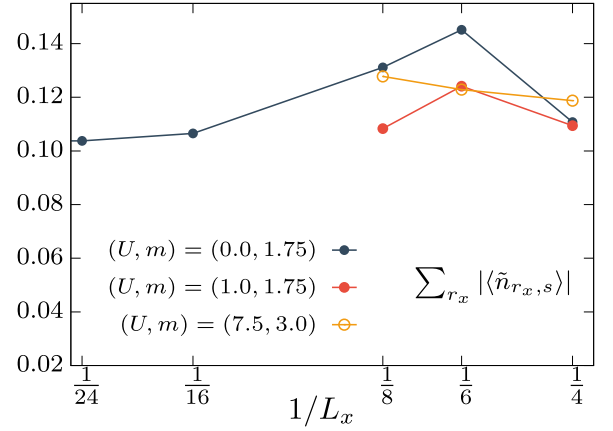


FIG. 12. Finite-size scaling analysis of the edge density for $(U, m) = (0.0, 1.75)$ (system sizes up to 24×4), $(U, m) = (1.0, 1.75)$ (systems up to 8×4), and $(U, m) = (7.5, 3.0)$ (systems up to 8×4) all of which lies in the paramagnetic T_1 topological phase. The plot is obtained by taking the average area under curve of the edge electronic density, $\langle \tilde{n}_{r_x, s} \rangle = \sum_{r_y} \langle \tilde{n}_{r_x, r_y, s} \rangle / L_y$ and depicts robustness of the edge signals of orbital s as we move towards larger system sizes.

interactions. It is then the competition that occurs between the U' , which explicitly pushes the system towards a mixed band insulator of $(0, 2)$ and $(2, 0)$ configuration, and the Hund's coupling and pair hopping term, which forces the system towards the $(1, 1)$ configuration that governs the magnetic transitions in the intermediate interacting regime [14].

The eigenvalues and corresponding eigenvectors of the matrix Hamiltonian in (A2) are

$$\begin{aligned} E_{B_1} &= U - \sqrt{J_H^2 + 4m^2}, & |B_1\rangle &= \gamma |\uparrow\downarrow, 0\rangle + \delta |0, \uparrow\downarrow\rangle, \\ E_{B_2} &= U + \sqrt{J_H^2 + 4m^2}, & |B_2\rangle &= \delta |\uparrow\downarrow, 0\rangle - \gamma |0, \uparrow\downarrow\rangle, \\ E_S &= U - J_H, & |S\rangle &= \frac{1}{\sqrt{2}} [|\downarrow, \uparrow\rangle - |\uparrow, \downarrow\rangle], \\ E_T &= U - 3J_H, & |T\rangle &= \frac{1}{\sqrt{2}} [|\downarrow, \uparrow\rangle + |\uparrow, \downarrow\rangle], \end{aligned} \quad (\text{A3})$$

where $|B_1\rangle$ and $|B_2\rangle$ are two band insulating states formed by the linear combinations of $(n_s, n_p) = (0, 2)$ and $(2, 0)$ configurations, with coefficients $\gamma = -J_H$ and $\delta = 2m + \sqrt{J_H^2 + 4m^2}$. The states $|S\rangle$ and $|T\rangle$ are the spin-singlet and triplet states with $S_{\text{tot}}^z = 0$, formed by the $(1, 1)$ configurations. Other than the triplet state all three states have zero magnetic moments and thus are nonmagnetic.

In Fig. 10, we plot the above four eigenvalues for $m = 3.0$. The plot clearly demonstrates that, from weaker to intermediate values of U the ground-state lies in the nonmagnetic band insulator phase in form of the $|B_1\rangle$ state, and as it reaches the intermediate interacting regime it transitions to the magnetic triplet state $|T\rangle$, which continues to the strongly interacting regime. The transition from the $|B_1\rangle$ state to $|T\rangle$ state occurs at $U = 2\sqrt{2}m$, for $m = 3.0$ it happens at $U = 8.485 (\simeq 8.5)$.

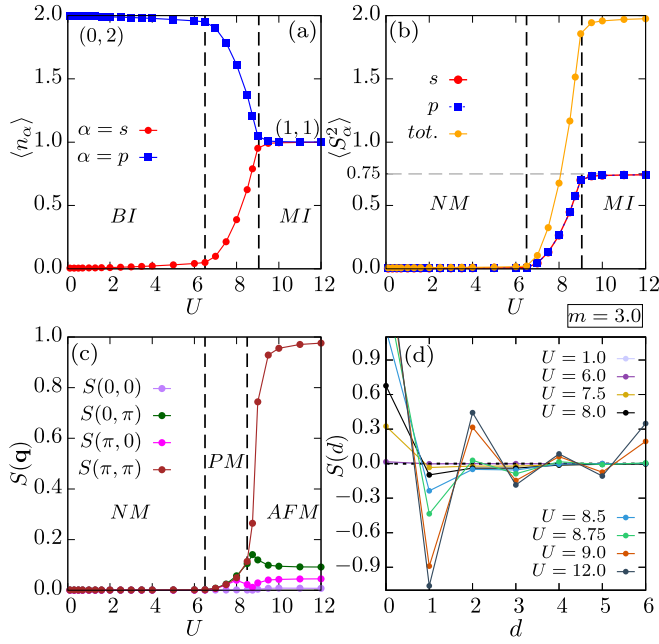


FIG. 13. Charge and magnetic properties of the interacting BHZ model with $m = 3.0$, $U > 0$ on a 4×4 cylinder. (a) Average orbital occupation vs U for both s and p orbitals, revealing a change in orbital occupation from a (0,2) BI configuration to (1,1) MI configuration with increasing interaction strength. (b) Average magnetic moment of a orbitals and of the entire cell are plotted vs U , showcasing a magnetic transition from a NM phase to a magnetic phase at $U = 6.5$. (c) The spin structure factor plot demonstrating the transition from NM to PM to AFM phase as we increase U . (d) Real-space spin-spin correlations vs the scalar distance between spins. These findings are consistent with our results at the same parameters for an 8×4 system shown in Fig. 4.

Moreover, this transition point is consistently close to our DMRG phase boundary between the paramagnetic and anti-ferromagnetic phase in Fig. 8.

APPENDIX B: FINITE-SIZE SCALING

To explore the robustness of DMRG results on finite cylinders, we conducted a finite-size scaling analysis of the observed topological phases. Figure 11 presents the edge electronic charge density for 8×4 and 4×4 cylinders at $U = 7.0$ and $m = 3.0$, which correspond to the paramagnetic T_1 phase. The results clearly show that the edge density signal in the 8×4 cylinder are consistent and more robust as compared to the 4×4 case. This consistency establishes the reliability of our topological marker as well as the separation between edge and bulk properties.

To obtain more systematic information on finite-size effects for the edge densities, we calculated $\langle \tilde{n}_{i,s} \rangle = \sum_{r_y} \langle \tilde{n}_{r_x, r_y, s} \rangle / L_y$, for three different set of parameters $(U, m) = (0.0, 1.75)$, $(1.0, 1.75)$, $(7.5, 3.0)$ from the PM T_1 phase with the results shown in Fig. 12. The plot illustrates that the signal at $(U, m) = (0.0, 1.75)$ saturates to a finite value as we increase the size of the cylinder along the x axis. More importantly, we observe a similar behavior in the presence

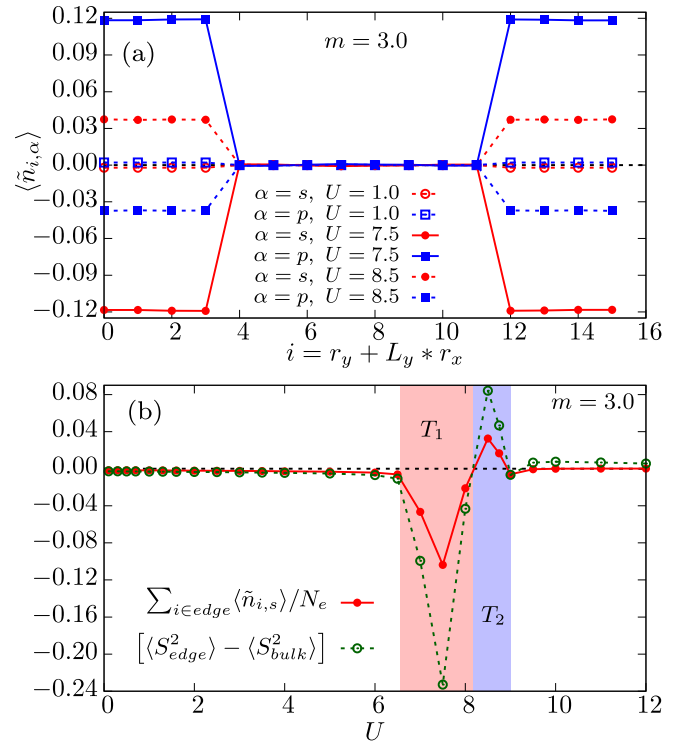


FIG. 14. Topological properties of the interacting BHZ model at $m = 3.0$ for a 4×4 cylinder. (a) The plot of edge electronic charge density vs the cell index i for different values of $U = 1.0, 7.5, 8.5$. The plot shows that the parameter point $U = 1.0$ is nontopological or trivial, whereas the parameter points $U = 7.5$ and $U = 8.5$ corresponds to the T_1 and T_2 topological phases, respectively. (b) Average edge density for orbital s and the difference of edge and bulk magnetic moments vs U , depicting a change in polarity of the edge density as distinguishing the T_1 and T_2 topological phases. The findings are consistent with our topological results at the same parameter for 8×4 system in Fig. 6.

of interactions for both $(U, m) = (1.0, 1.75)$ and $(U, m) = (7.5, 3.0)$ where DMRG calculations are computationally costly.

APPENDIX C: 4×4 RESULTS AT $m = 3.0$

For the case of $m = 3.0$, we have performed DMRG simulations for both 8×4 and 4×4 cylinders over all interaction strengths. We observed that in both cases, the magnetic and topological properties are remarkably consistent, indicating the reliability of our DMRG determined phase diagram

This can be clearly illustrated through Figs. 13 and 4, which depict the charge and magnetic properties of a 4×4 and 8×4 cylinders, respectively, at $m = 3.0$. In both cases, the presence of different magnetic phases, and their ordering and transitions as we increase U , are consistent with each other. Similarly for the topological properties, a side-by-side comparison between Fig. 14(b) and Fig. 6(b) confirms the persistence and robustness of the T_1 and T_2 topological phases, across both cylinder sizes, within the

framework of our DMRG calculations for the interacting BHZ model.

APPENDIX D: ENTANGLEMENT SPECTRUM

The entanglement spectrum of the system can be obtained from the Schmidt decomposition of the many-body ground state $|\Psi\rangle = \sum_{\alpha} \lambda_{\alpha} |L, \alpha\rangle \otimes |R, \alpha\rangle$, where $|L, \alpha\rangle (|R, \alpha\rangle)$ corresponds to the left(right) partitions of the system and λ_{α}^2 are the eigenvalues of the spatially reduced density matrix $\rho_L = \text{Tr}_R |\Psi\rangle\langle\Psi|$ of the partition [56]. Analyzing the eigenvalues can facilitate distinguishing between topological and nontopological phases, as demonstrated previously in 1D systems [57]. However, it is not a universal indicator for characterizing distinct phases [58]. Figure 15 shows a plot of the low-level entanglement spectrum with $m = 3.0$ on an 8×4 cylinder for various values of U , corresponding to different phases. The entanglement levels are obtained by diagonalizing the reduced density matrix for a center cut dividing the cylinder in two, where the cut is acting like an edge in the y direction. In the band insulator spectrum seen in panel (a) for $U = 1.0$, we observe a single low-lying eigenvalue corresponding to the entanglement in the ground state separated by a large gap to several fourfold degenerate excited states. In case of the PM T_1 and SAFM T_2 phase, which are plotted for $U = 7.0$ and $U = 8.5$ as panels (b) and (c) we observe a doubly degenerate excited level corresponding to the helical nature of edge states. In panel (d), the emergence of long-range antiferromagnetic order breaks time-reversal symmetry and leads to a splitting that is seen in the nondegenerate excited entanglement levels.

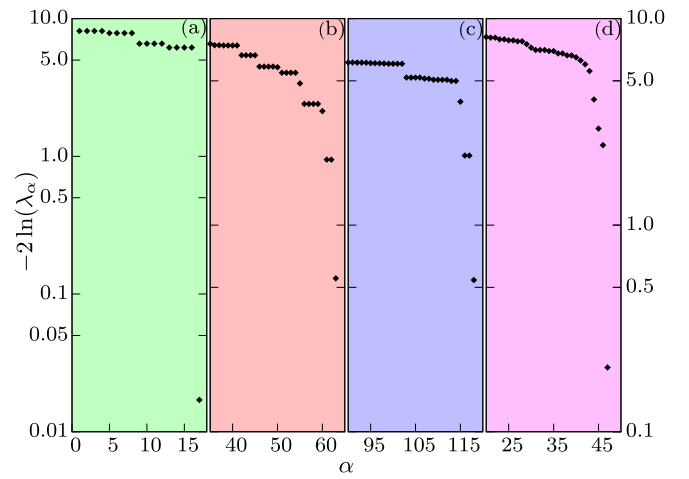


FIG. 15. The low-level entanglement spectrum on an 8×4 cylinder at a fixed $m = 3.0$ is illustrated for different values of U , corresponding to various phases in our study. In (a) we present the entanglement spectrum for $U = 1.0$ for the band insulator, (b) $U = 7.0$ from the paramagnetic topological T_1 (Paramagnetic T_1) phase, (c) displays the entanglement spectrum for $U = 8.5$ from the SAFM T_2 (stripey-antiferromagnetic T_2) phase, and (d) depicts the entanglement spectrum for $U = 11.0$ from the AFM MI (antiferromagnetic Mott insulator) region. The y axis on the left pertains to panel (a), while the right y axis applies to panels (b)–(d). The plot highlights the presence of degenerate density matrix eigenvalues in the first excited state of the spectrum: fourfold degenerate in the BI phase, twofold in both the T_1 and T_2 phases, with the MI phase showing nondegeneracy.

-
- [1] M. Z. Hasan and C. L. Kane, *Rev. Mod. Phys.* **82**, 3045 (2010).
 [2] X.-L. Qi and S.-C. Zhang, *Rev. Mod. Phys.* **83**, 1057 (2011).
 [3] X.-G. Wen, *Rev. Mod. Phys.* **89**, 041004 (2017).
 [4] C. L. Kane and E. J. Mele, *Phys. Rev. Lett.* **95**, 226801 (2005).
 [5] B. A. Bernevig, T. L. Hughes, and S.-C. Zhang, *Science* **314**, 1757 (2006).
 [6] C. Wu, B. A. Bernevig, and S.-C. Zhang, *Phys. Rev. Lett.* **96**, 106401 (2006).
 [7] B. A. Bernevig and S.-C. Zhang, *Phys. Rev. Lett.* **96**, 106802 (2006).
 [8] C. Xu and J. E. Moore, *Phys. Rev. B* **73**, 045322 (2006).
 [9] C. L. Kane and E. J. Mele, *Phys. Rev. Lett.* **95**, 146802 (2005).
 [10] M. König, S. Wiedmann, C. Brune, A. Roth, H. Buhmann, L. W. Molenkamp, X.-L. Qi, and S.-C. Zhang, *Science* **318**, 766 (2007).
 [11] S. Rachel, *Rep. Prog. Phys.* **81**, 116501 (2018).
 [12] L. Wang, X. Dai, and X. C. Xie, *Europhys. Lett.* **98**, 57001 (2012).
 [13] Y. Tada, R. Peters, M. Oshikawa, A. Koga, N. Kawakami, and S. Fujimoto, *Phys. Rev. B* **85**, 165138 (2012).
 [14] J. C. Budich, B. Trauzettel, and G. Sangiovanni, *Phys. Rev. B* **87**, 235104 (2013).
 [15] A. Amaricci, J. C. Budich, M. Capone, B. Trauzettel, and G. Sangiovanni, *Phys. Rev. Lett.* **114**, 185701 (2015).
 [16] S. Miyakoshi and Y. Ohta, *Phys. Rev. B* **87**, 195133 (2013).
 [17] T. Yoshida, R. Peters, S. Fujimoto, and N. Kawakami, *Phys. Rev. B* **87**, 085134 (2013).
 [18] A. Amaricci, A. Valli, G. Sangiovanni, B. Trauzettel, and M. Capone, *Phys. Rev. B* **98**, 045133 (2018).
 [19] Y. Ren, Z. Qiao, and Q. Niu, *Phys. Rev. Lett.* **124**, 166804 (2020).
 [20] Z. Chen and T. K. Ng, *Phys. Rev. B* **99**, 235157 (2019).
 [21] F. Dominguez, B. Scharf, and E. M. Hankiewicz, *SciPost Phys. Core* **5**, 024 (2022).
 [22] S. Saha, and A. Mawrie, *arXiv:2208.13491*.
 [23] F. Xue and A. H. MacDonald, *Phys. Rev. Lett.* **120**, 186802 (2018).
 [24] P. Mai, B. E. Feldman, and P. W. Phillips, *Phys. Rev. Res.* **5**, 013162 (2023).
 [25] P. Mai, J. Zhao, B. E. Feldman, and P. W. Phillips, *Nat. Commun.* **14**, 5999 (2023).
 [26] B. Roy, P. Goswami, and J. D. Sau, *Phys. Rev. B* **94**, 041101(R) (2016).
 [27] J. Wang, Y. Meir, and Y. Gefen, *Phys. Rev. Lett.* **118**, 046801 (2017).
 [28] A. Amaricci, L. Privitera, F. Petocchi, M. Capone, G. Sangiovanni, and B. Trauzettel, *Phys. Rev. B* **95**, 205120 (2017).

- [29] N. John, A. D. Maestro, and B. Rosenow, *Europhys. Lett.* **140**, 26002 (2022).
- [30] S.-S. Gong, W. Zhu, and D. N. Sheng, *Sci. Rep.* **4**, 6317 (2014).
- [31] W.-J. Hu, S.-S. Gong, H.-H. Lai, Q. Si, and E. Dagotto, *Phys. Rev. B* **101**, 014421 (2020).
- [32] S. Jiang, D. J. Scalapino, and S. R. White, *Proc. Natl. Acad. Sci. USA* **118**, e2109978118 (2021).
- [33] C. Peng, Y.-F. Jiang, Y. Wang, and H.-C. Jiang, *New J. Phys.* **23**, 123004 (2021).
- [34] H.-C. Jiang, and S. A. Kivelson, *Proc. Natl. Acad. Sci. USA* **119**, e2109406119 (2021).
- [35] C. Peng, Y. Wang, J. Wen, Y. S. Lee, T. P. Devereaux, and H.-C. Jiang, *Phys. Rev. B* **107**, L201102 (2023).
- [36] J. Kanamori, *Prog. Theor. Phys.* **30**, 275 (1963).
- [37] N. D. Patel, A. Nocera, G. Alvarez, A. Moreo, and E. Dagotto, *Phys. Rev. B* **96**, 024520 (2017).
- [38] N. D. Patel, N. Kaushal, A. Nocera, G. Alvarez, and E. Dagotto, *npj Quantum Mater.* **5**, 27 (2020).
- [39] R. Soni, N. Kaushal, C. Şen, F. A. Reboredo, A. Moreo, and E. Dagotto, *New J. Phys.* **24**, 073014 (2022).
- [40] S. R. White, *Phys. Rev. Lett.* **69**, 2863 (1992).
- [41] U. Schollwöck, *Rev. Mod. Phys.* **77**, 259 (2005).
- [42] G. Alvarez, *Comput. Phys. Commun.* **180**, 1572 (2009).
- [43] L. Ziegler, E. Tirrito, M. Lewenstein, S. Hands, and A. Bermudez, *Ann. Phys.* **439**, 168763 (2022).
- [44] L. Ziegler, E. Tirrito, M. Lewenstein, S. Hands, and A. Bermudez, *arXiv:2011.08744*.
- [45] D. Nanclares, L. R. F. Lima, C. H. Lewenkopf, and L. G. G. V. Dias da Silva, *Phys. Rev. B* **96**, 155302 (2017).
- [46] S. S. Krishtopenko and F. Teppe, *Phys. Rev. B* **97**, 165408 (2018).
- [47] A. M. Essin and V. Gurarie, *Phys. Rev. B* **84**, 125132 (2011).
- [48] P. Werner and A. J. Millis, *Phys. Rev. Lett.* **99**, 126405 (2007).
- [49] L. Wang, *Phys. Rev. B* **94**, 195105 (2016).
- [50] S. J. Wetzel, *Phys. Rev. E* **96**, 022140 (2017).
- [51] C. Wang and H. Zhai, *Phys. Rev. B* **96**, 144432 (2017).
- [52] S. Acevedo, M. Arlego, and C. A. Lamas, *Phys. Rev. B* **103**, 134422 (2021).
- [53] F. Pedregosa, G. Varoquaux, A. Gramfort, V. Michel, B. Thirion, O. Grisel, M. Blondel, P. Prettenhofer, R. Weiss, V. Dubourg *et al.*, *J. Mach. Learn. Res.* **12**, 2825 (2011).
- [54] R. Soni and A. Del Maestro, All code, scripts and data used in this paper are included in a GitHub repository: <https://github.com/DelMaestroGroup/papers-code-interactingBHZmodel>.
- [55] G. Alvarez, DMRG++ Website, <https://g1257.github.io/dmrgPlusPlus/>.
- [56] H. Li and F. D. M. Haldane, *Phys. Rev. Lett.* **101**, 010504 (2008).
- [57] F. Pollmann, A. M. Turner, E. Berg, and M. Oshikawa, *Phys. Rev. B* **81**, 064439 (2010).
- [58] A. Chandran, V. Khemani, and S. L. Sondhi, *Phys. Rev. Lett.* **113**, 060501 (2014).